Gen Relativ Gravit (2012) 44:509–533
DOI 10.1007/s10714-011-1289-0

RESEARCH ARTICLE

Detailed study of null and timelike geodesics in the Alcubierre warp spacetime

Thomas Müller · Daniel Weiskopf

Received: 11 August 2011 / Accepted: 18 October 2011 / Published online: 5 November 2011

Abstract The geodesic equation of the Alcubierre warp spacetime is converted into its non-affinely parametrized form for a detailed discussion of the motion of particles and the visual effects as observed by a traveller inside the warp bubble or a person looking from outside. To include gravitational lensing for point-like light sources, we present a practical approach using the Jacobi equation and the Sachs bases. Additionally, we consider the dragging and geodesic precession of particles due to the warp bubble.

Keywords Alcubierre warp spacetime · Non-affinely parametrized geodesics · Relativistic visualization

1 Introduction

Spacetimes associated with exotic matter like the Morris-Thorne [1] wormhole and the Alcubierre warp metric [2] offer a rich field for studying geodesics in extreme application cases of general relativity. While geodesics in the Morris–Thorne wormhole can be handled numerically in a quite straightforward manner, the time-dependent Alcubierre spacetime yields numerically unstable integration of the geodesic equation, the equation for the parallel transport of vectors along timelike geodesics, and the equations to determine the gravitational lensing effect caused by the warp bubble if those equations are used in their standard parameterization.

T. Müller (✉) · D. Weiskopf
Visualisierungsinstitut der Universität Stuttgart (VISUS), Allmandring 19,
70569 Stuttgart, Germany
e-mail: Thomas.Mueller@visus.uni-stuttgart.de

D. Weiskopf
e-mail: Daniel.Weiskopf@visus.uni-stuttgart.de

This paper deals with the warp metric of Alcubierre. We study in detail the influence of the warp bubble on null and timelike geodesics. For that, we first transform all the relevant equations mentioned above into their non-affinely parametrized form. Here, we use the coordinate time as non-affine parameter. This makes the equations numerically more practical and more robust than their affinely parametrized form, especially in the neighborhood of the warp bubble's rim. Beside the paths of light rays, we also discuss the frequency shift and the effect on a bundle of light rays resulting in gravitational lensing of point-like objects. Furthermore, we explain what an observer would actually see inside or outside the warp bubble using four-dimensional ray tracing. By means of the parallel-transport equation, we show how particles initially at rest will be carried along and undergo geodesic precession.

A detailed discussion of the paths of null geodesics and their frequency shift as observed from inside the Alcubierre warp bubble, in particular the emergence of an apparent horizon behind the warp bubble, was given by Clark et al. [3]. The influence of a warp bubble passing between the observer and a distant object onto the visual distortion was studied by Weiskopf [4] using four-dimensional raytracing. In our paper, we will pick up the ideas by Clark et al. and Weiskopf making them numerically more robust and adding the gravitational lensing aspect and the motion of particles.

There are several papers that discuss the physical nature of warp drive spacetimes, and we can give only a few references [5–8]. To study geodesics in detail, we refer the reader to the interactive visualization tool *GeodesicViewer* [9].

The structure of this paper is as follows. In Sect. 2, we briefly review the Alcubierre warp metric and present the local reference frames of a comoving and a static observer. In Sect. 3, we study the trajectories of light rays and how they influence the view of an observer that either co-moves with the warp bubble or stays static in the outside. We also discuss the frequency shift and the lensing effect caused by the warp bubble.

Finally, we investigate the influence of the warp bubble on particle trajectories in Sect. 4. The technical details of the conversion and the integration of the non-affinely parametrized equations are relegated to the Appendix.

An accompanying Java application that shows the view of the stellar sky from inside the warp bubble, high-resolution images of this article, as well as some movies that show the visual distortion of the warp bubble or the motion of particles can be downloaded from http://www.vis.uni-stuttgart.de/relativity.

2 Warp metric and local reference frames

The Warp metric developed by Miguel Alcubierre [2] can be described by the line element

$$ds^2 = -c^2 dt^2 + [dx - vf(r)dt]^2 + dy^2 + dz^2, \tag{1}$$

where c is the speed of light, $v = dx(t)/dt$,

$$r(t) = \sqrt{(x - x(t))^2 + y^2 + z^2}, \quad f(r) = \frac{\tanh(\sigma(r + R)) - \tanh(\sigma(r - R))}{2\tanh(\sigma R)}, \tag{2}$$

and $x(t)$ is the worldline of the center of the warp bubble. The parameters $R > 0$ and $\sigma > 0$ in the shape function $f(r)$ define the radius and the thickness of the bubble. The Christoffel symbols are listed in "Appendix A".

For the warp metric, we can define two natural local tetrads $\mathbf{e}_{(i)} = e^{\mu}_{(i)}\partial_\mu$ that represent the local reference frames of either a comoving or a static observer. The comoving tetrad is defined by

$$\mathbf{e}_{(0)} = \frac{1}{c}(\partial_t + vf\partial_x), \quad \mathbf{e}_{(1)} = \partial_x, \quad \mathbf{e}_{(2)} = \partial_y, \quad \mathbf{e}_{(3)} = \partial_z, \tag{3}$$

and the static local tetrad reads

$$\hat{\mathbf{e}}_{(0)} = \frac{1}{\sqrt{c^2 - v^2 f^2}}\partial_t, \quad \hat{\mathbf{e}}_{(1)} = -\frac{vf}{c\sqrt{c^2 - v^2 f^2}}\partial_t + \frac{\sqrt{c^2 - v^2 f^2}}{c}\partial_x, \quad \hat{\mathbf{e}}_{(2)} = \partial_y, \quad \hat{\mathbf{e}}_{(3)} = \partial_z. \tag{4}$$

It is obvious that the comoving tetrad is valid everywhere, whereas the static tetrad is defined only in the region of the spacetime where $v^2 f^2 < c^2$. Both tetrads fulfill the orthonormality condition $g_{\mu\nu}e^{\mu}_{(i)}e^{\nu}_{(j)} = \eta_{(i)(j)}$ with $\eta_{(i)(j)} = \mathrm{diag}(-1, 1, 1, 1)$, which means that these tetrads locally define a Minkowski system.

Throughout the paper we consider a warp bubble that moves with constant velocity. Thus, the center of the warp bubble follows the worldline $x(t) = vt$. Furthermore, we set $\{c\} = 1$ for numerical examples. Then, times and distances are given in seconds and light-seconds or years and light-years, respectively.

3 Null geodesics

In this section, we will discuss the influence of the warp bubble on the propagation of light for several different situations. For the numerical integration of the geodesic equation in the warp metric, an integrator with step-size control is indispensable. Otherwise, the step-size would have to be inefficiently tiny. However, irrespective of the numerical integrator, direct integration of the geodesic equation leads to numerical problems at the rim of the bubble for certain initial values because of the inappropriate affine parameter. Although the spacetime coordinates (t, x, y, z) are smooth, the step-size of the affine parameter becomes extremely small. Thus, an integrator with step-size control will get stuck and the constraint equation will be violated. To avoid the numerical difficulties, we use the non-affinely parametrized geodesic as described in "Appendix B". Additionally, the resulting equations are numerically much more accurate than the ones that follow from the affinely parametrized geodesic equation. Here, we use the coordinate time t as non-affine parameter.

The gravitational frequency shift z_f between the emitted, ω_{src}, and the observed, ω_{obs}, light frequencies is obtained by

$$1 + z_f = \frac{\omega_{\text{src}}}{\omega_{\text{obs}}} = \frac{g_{\mu\nu}u^\mu k^\nu\big|_{\text{src}}}{g_{\mu\nu}u^\mu k^\nu\big|_{\text{obs}}}, \qquad k^\mu = \frac{dx^\mu}{d\lambda}, \tag{5}$$

see e.g., Wald [10]. If $-1 < z_f < 0$, we call it a blueshift, and if $z_f > 0$, it is a redshift.

To determine the lensing effect caused by the warp bubble, we study the behavior of the spacetime curvature on a bundle of light rays that is described by two Jacobian fields $\mathbf{Y}_i = Y_i^\mu \partial_\mu$. The change of the Jacobian fields along the central light ray with tangent $\mathbf{k} = k^\mu \partial_\mu$ is determined by the Jacobian equation

$$\frac{D^2 Y_i^\mu}{d\lambda^2} = R^\mu_{\nu\rho\sigma} k^\nu k^\rho Y_i^\sigma. \tag{6}$$

The cross section of the light bundle follows from the projection of the Jacobian fields onto the parallel-transported Sachs vectors $\mathbf{s}_i = s_i^\mu \partial_\mu$ that are perpendicular to the light ray $\mathbf{k}$. The resulting Jacobi matrix

$$J_{ij} = g_{\mu\nu} Y_i^\mu s_j^\nu \tag{7}$$

describes how the shape of the initially circular bundle of light rays transforms into an ellipse with major and minor axes $a_\pm$ along the central light ray. Fortunately, we can calculate the matrix by first integrating from the observer to the source and then inverting this matrix to obtain the behavior of a light bundle from the source to the observer. The result of this calculation is the magnification factor $\mu_{\text{mag}} = \lambda^2/(a_+ a_-)$. A practical approach to the calculation of the lensing effect in the context of the non-affinely parametrized equations can be found in “Appendix C”. A thorough discussion of gravitational lensing, however, is out of the scope of this article and we refer the reader to the standard literature [11].

3.1 View from the bridge

The bending of light as well as the frequency shift for an observer at the center of the warp bubble (view from the bridge) was already discussed in detail by Clark et al. [3]. What is not known so far is how the warp bubble influences the lensing of point-like objects. Hence, we first reconstruct the results of Clark et al. for the sake of completeness and then calculate the lensing effect.

The local reference frame of the bridge is given by the comoving tetrad of Eq. (3). Because of the axial symmetry, we can restrict to geodesics in the xy-plane. Then, an incident light ray with angle ξ with respect to the local reference frame can be

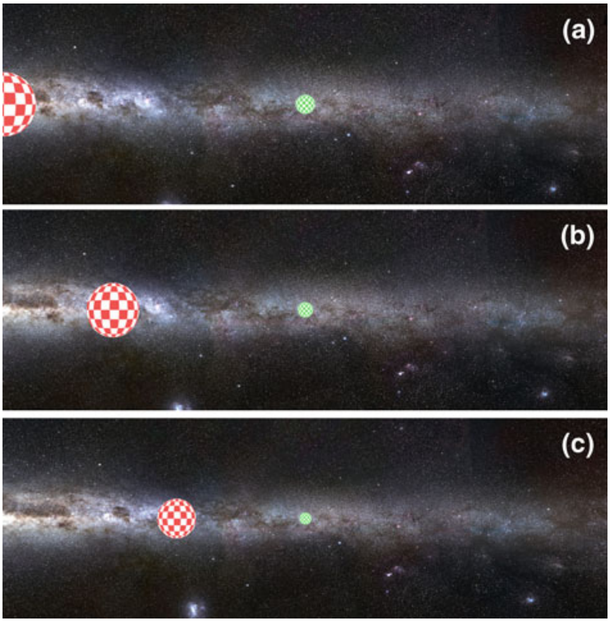

Fig. 1 View from the bridge at $t = 0$ in the direction of motion for velocities $v = 0.01c$ (**a**), $v = c$ (**b**), $v = 2c$ (**c**) and a panorama camera with $180° \times 60°$ field of view. Here, only the geometric distortion is shown. The Milky Way background is represented by a sphere with radius $r_{\max} = 200$ [12]

described by the four vector

$$\mathbf{k} = \omega \left(-\mathbf{e}_{(0)} + \cos\xi\,\mathbf{e}_{(1)} + \sin\xi\,\mathbf{e}_{(2)}\right) = k^\mu \partial_\mu. \tag{8}$$

Here, we use the minus sign in front of the timelike tetrad vector $\mathbf{e}_{(0)}$ because we integrate geodesics back in time. If we are only interested in the paths of the light rays, we can set the frequency $\omega = 1$.

Figure 1 shows the view from the bridge of an observer moving with different warp speeds when passing the origin $x = y = 0$ at $t = 0$. To visualize distortion effects close to the warp bubble, we use two checkered balls of radius $r_{\text{ball}} = 0.5$. The green ball is located at $x = 10$, $y = 0$ whereas the red ball is located at $x = 0$, $y = 3$. Similar to the special relativistic motion in flat Minkowski spacetime, there is an aberration in the direction of motion that is stronger the faster the warp bubble moves. In contrast to the special relativistic motion, however, the aberration here is only due to the curved spacetime.

As already found by Clark et al. [3] there is no aberration for $\xi = 90°$. Hence, light rays that originate precisely at 90° to the direction of motion of the warp bubble will be seen by an observer at the bridge at an angle $\xi = 90°$ (see also "Appendix D"). Furthermore, the observer on the bridge cannot see the whole spacetime. If we trace light rays from the bridge with initial angles ξ back in time until they hit a sphere in the asymptotic background, $r = r_{\max}$, cf. Fig. 2, we find that there is an apparent horizon opposite to the direction of motion, where the size of the apparent horizon depends

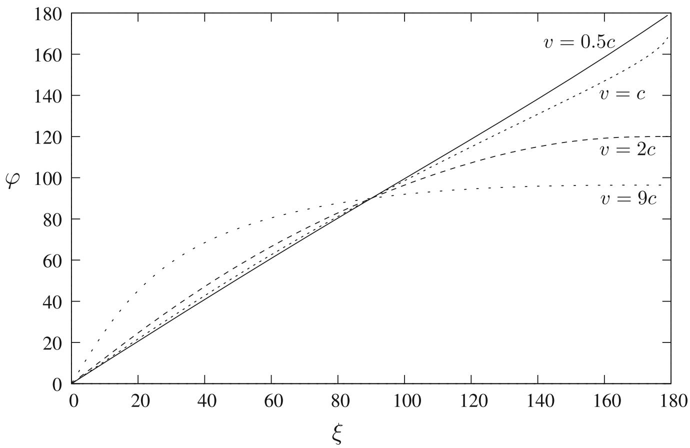

Fig. 2 Angle φ at $r_{\max} = 5 \times 10^4$ with respect to the incident angle ξ for velocities $v/c = \{0.5, 1, 2, 9\}$ and warp parameters $R = 2$, $\sigma = 1$. The angle $\xi = 0°$ corresponds to the direction of motion. For the observer with $v = 9c$, the region with $\varphi \approx 96° \ldots 180°$ is not visible

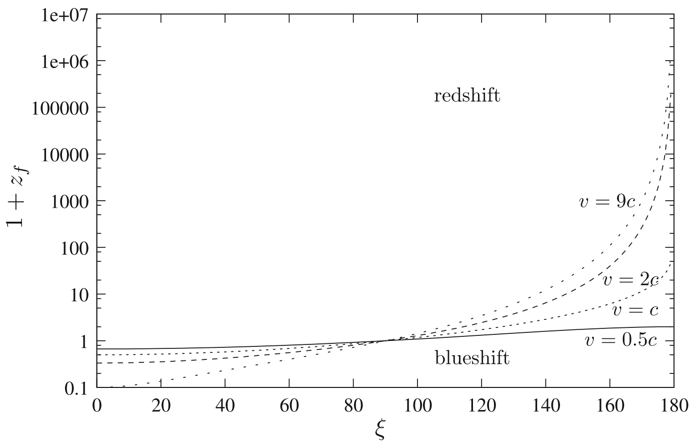

Fig. 3 Frequency shift $1 + z_f$ between $r_{\max} = 5 \times 10^4$ and the bridge with respect to the incident angle ξ for velocities $v/c = \{0.5, 1, 2, 9\}$ and warp parameters $R = 2$, $\sigma = 1$. The angle $\xi = 0°$ corresponds to the direction of motion

on the velocity of the warp bubble. However, the observer will not see a black region because for any direction ξ some region of the asymptotic background will be visible.

To determine the frequency shift and the lensing caused by the warp bubble, we use the asymptotic sphere as the place where there are everywhere point-like light sources with unit frequency $\omega_{\text{src}} = 1$. Then, the observer at the bridge will detect frequency shifts as shown in Fig. 3. Irrespective of the velocity, there is no frequency shift for $\xi = 90°$. In the direction of motion, $\xi < 90°$, we have a slight blueshift, whereas in the opposite direction the redshift is quite strong.

The lensing of point-like sources caused by the warp bubble is shown in Fig. 4. In the direction of motion, we have a slight magnification, whereas in the opposite

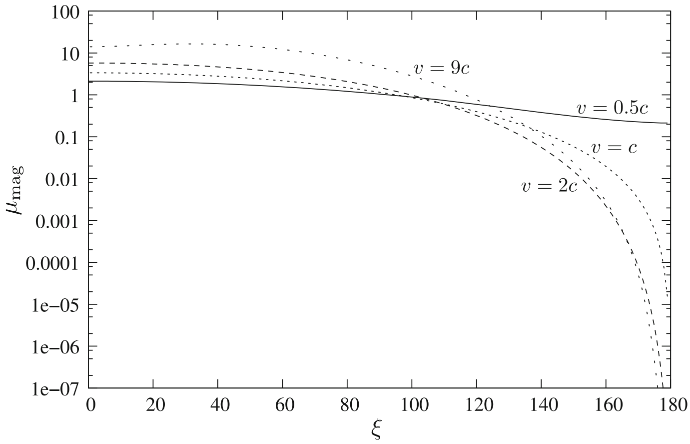

Fig. 4 Lensing μ_{mag} between $r_{\mathrm{max}} = 5 \times 10^4$ and the bridge with respect to the incident angle ξ for velocities $v/c = \{0.5, 1, 2, 9\}$ and warp parameters $R = 2, \sigma = 1$. The angle $\xi = 0°$ corresponds to the direction of motion

direction, the light of point-like sources are strongly dimmed. Hence, even though the horizon does not produce a black region, the strong redshift together with the magnification let the region $\xi > 90°$ appear dark for high velocities.

The 'view from the bridge' for a special-relativistically moving observer is well-known from standard literature. The aberration and Doppler-shift can be derived from the representation of an initial direction $\mathbf{k}$ with respect to either the moving reference frame

$$\bar{\mathbf{e}}_{(0)} = \frac{\gamma}{c}\left(\partial_t + v_{\mathrm{sr}}\partial_x\right), \quad \bar{\mathbf{e}}_{(1)} = \gamma\left(\frac{v_{\mathrm{sr}}}{c^2}\partial_t + \partial_x\right), \quad \bar{\mathbf{e}}_{(2)} = \partial_y, \quad \bar{\mathbf{e}}_{(3)} = \partial_z, \tag{9}$$

as in Eq. (8), or the standard Minkowski frame. Here, v_{sr} is the special-relativistic velocity of the moving observer. Thus, we obtain the aberration formula

$$\cos\xi' = \frac{\gamma}{D}\left(\cos\bar{\xi} - v_{\mathrm{sr}}/c\right) \tag{10}$$

and the Doppler-shift

$$1 + z_f = D, \tag{11}$$

where $D = \gamma[1 - (v_{\mathrm{sr}}/c)\cos\bar{\xi}]$ is the Doppler-factor and $\gamma = 1/\sqrt{1 - v_{\mathrm{sr}}^2/c^2}$. Here, the primed angle is with respect to the flat Minkowski spacetime and the barred angle is with respect to the special-relativistic reference frame. The magnification factor is given by

$$\mu_{\mathrm{mag}} = D^{-2}, \tag{12}$$

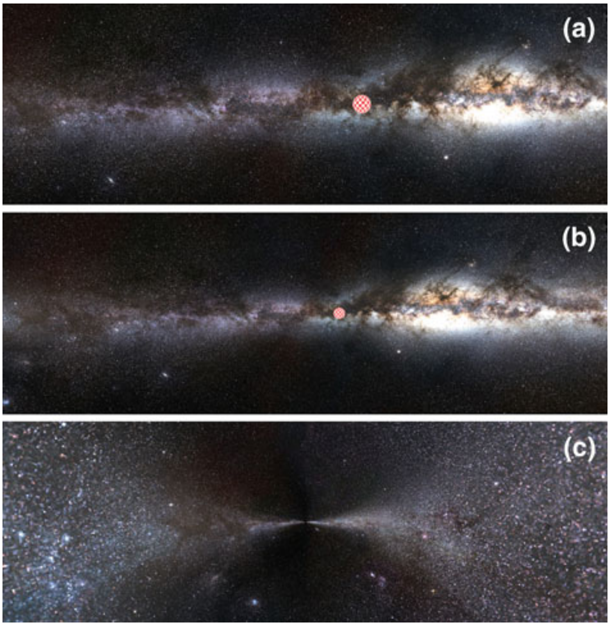

Fig. 5 View of a static observer located at $x = 10$, $y = 0$ in the negative x-direction towards the approaching warp bubble that moves with velocity $v = 2c$ and that crosses the origin $x = y = 0$ at $t = 0$. The panorama camera has $180° \times 60°$ field of view. The observation times are $t = \{0, 3.5, 3.98\}$ when the bubble is at $x_b = \{0, 7, 7.96\}$. The red ball is located at $x = 0$, $y = 3$. Here, only the geometric distortion is shown. The Milky Way background is represented by a sphere with radius $r_{\max} = 200$ [12]

see Weiskopf et al. [13] for a detailed discussion. For velocities $v_{\rm sr}$ close to the speed of light, we have very strong blueshift and huge magnification in the direction of motion.

While the direction of no frequency shift, $z_f = 0$, in the Warp metric is fixed by $\xi = 90°$, this borderline is defined by $D = 1$ in the special-relativistic case, which also gives the borderline of no-magnification, $\mu_{\rm mag} = 1$. The corresponding angle reads $\xi = \arccos\left[(\gamma - 1)/(\gamma v_{\rm sr}/c)\right]$, where $\xi < 90°$ for $v_{\rm sr} > 0$. Hence, for velocities close to the speed of light, a special-relativistic traveller will only see a small bright spot in contrast to a traveller inside a warp bubble.

3.2 Warp bubble approaching a static observer

Consider a static observer located at $x = 10$, $y = 0$ and a warp bubble with $R = 2$ and $\sigma = 1$ that approaches the static observer with $v = 2c$. At $t = 0$, the bubble crosses the origin $x = 0$, $y = 0$. The observer, however, that looks towards the approaching warp bubble, will not recognize any significant image distortion, see Fig. 5a. At $t = 3.5$ (Fig. 5b), the warp bubble is located at $x_{\rm b} = 7$ and, thus, is already quite close to the observer that will see that some portion of the sky apparently shrinks in the direction of view. However, in the next few instances the view of the observer changes

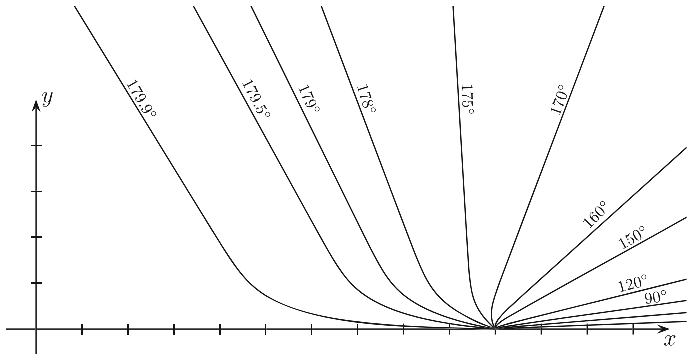

Fig. 6 Incoming light rays for a static observer at ($t = 3.98, x = 10, y = 0$) and warp parameters $R = 2, \sigma = 1$, and $v = 2c$

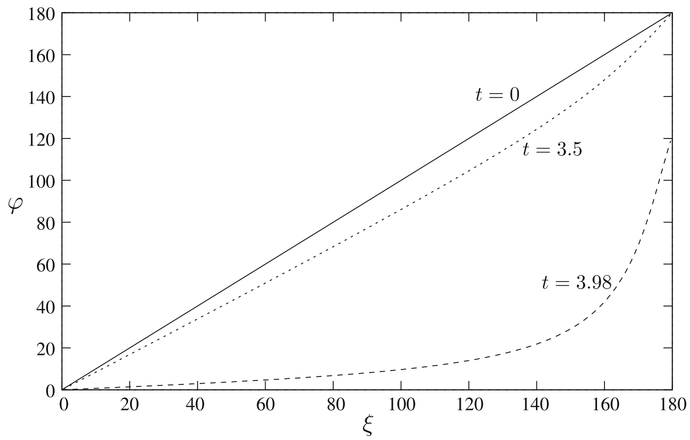

Fig. 7 Angle φ at $r_{\max} = 5 \times 10^4$ with respect to the incident angle ξ for a static observer at $x = 10, y = 0$ and $t = \{0, 3.5, 3.98\}$. The warp parameters read $R = 2, \sigma = 1$, and $v = 2c$. The angle $\xi = 180°$ corresponds to the direction of the approaching warp bubble

dramatically. Some parts of the sky in the direction of view disappear as a result of an apparent horizon like in the bridge observer example, see also Figs. 6 and 7.

The corresponding frequency shift and lensing diagrams are shown in Figs. 8 and 9. Here, $\xi = 180°$ represents the direction to the approaching warp bubble. For $t = 0$, there is no significant frequency shift or magnification in any direction. For $t = 3.98$ the warp bubble is located at $x_b = 7.96$, however, the approaching warp bubble leads to a strong blueshift in the direction of the warp bubble and a redshift in the opposite direction. The lensing effect lets stars appear brighter especially in the direction of the approaching warp bubble.

3.3 Warp bubble passing the observer

Consider a static observer located at $x = 0, y = -4$ and a warp bubble with parameters $R = 2, \sigma = 1$ that passes the observer with $v = 2c$. At $t = 0$, the bubble crosses

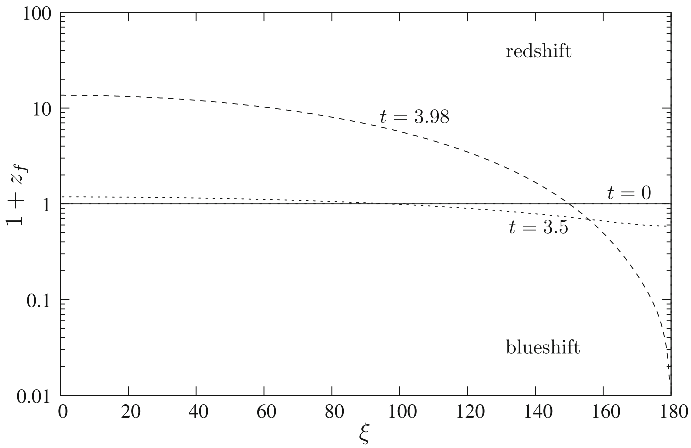

Fig. 8 Frequency shift $1+z_f$ between $r_{\mathrm{max}} = 5\times10^4$ and a static observer at $x = 10$, $y = 0$ and $t = \{0, 3.5, 3.98\}$. The warp parameters read $R = 2$, $\sigma = 1$, and $v = 2c$. Here, $\xi = 180°$ represents the direction to the approaching warp bubble

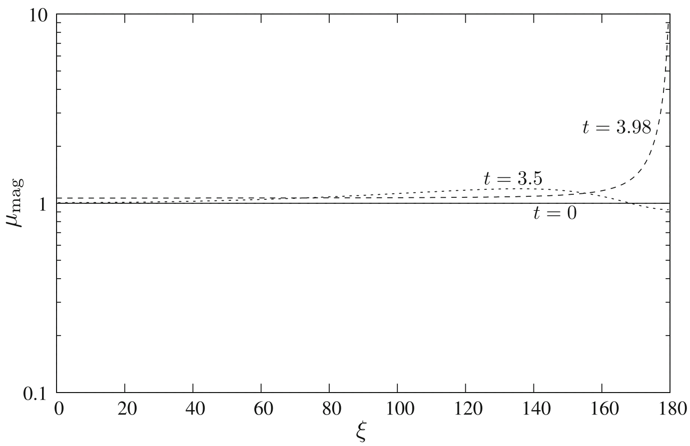

Fig. 9 Lensing μ_{mag} between $r_{\mathrm{max}} = 5\times10^4$ and a static observer at $x = 10$, $y = 0$ and $t = \{0, 3.5, 3.98\}$. The warp parameters read $R = 2$, $\sigma = 1$, and $v = 2c$. Here, $\xi = 180°$ represents the direction to the approaching warp bubble

the origin $x = 0$, $y = 0$. Figure 10 shows several representing light rays that reach the static observer at times $t = 3$ and $t = 6$ with incident angles $\xi = \{0°, 10°, \ldots, 180°\}$. The corresponding views for a panorama camera with $180°\times60°$ field of view heading towards the origin are shown in Fig. 11. Here, the Milky Way background is represented by a sphere with radius $r_{\mathrm{max}} = 200$, and the checkered ball of radius $r_{\mathrm{ball}} = 0.5$ is located at $x = 0$, $y = 3$.

The three phantom images of the ball (Fig. 11c) follow from light rays with incident angles $\xi \approx \{28.8°, 45°, 83.2°\}$. The distortion of the Milky Way background can be understood by means of the relation between the intersection angles φ of the light ray with the background sphere and the incident angles ξ, see Fig. 12. The discontinuities

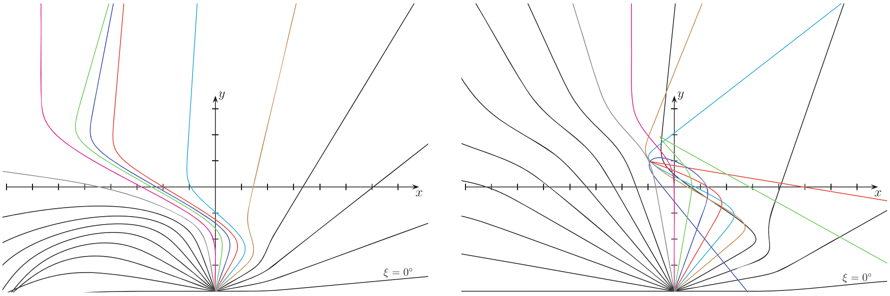

Fig. 10 Incoming light rays for a static observer located at ($x = 0$, $y = -4$) with incident angles $\xi = \{0°, 10°, \ldots, 180°\}$. The warp parameters read $R = 2$, $\sigma = 1$, and $v = 2c$. The colored lines are only for better distinguishability. The observation times are $t = 3$ (*left*) and $t = 6$ (*right*)

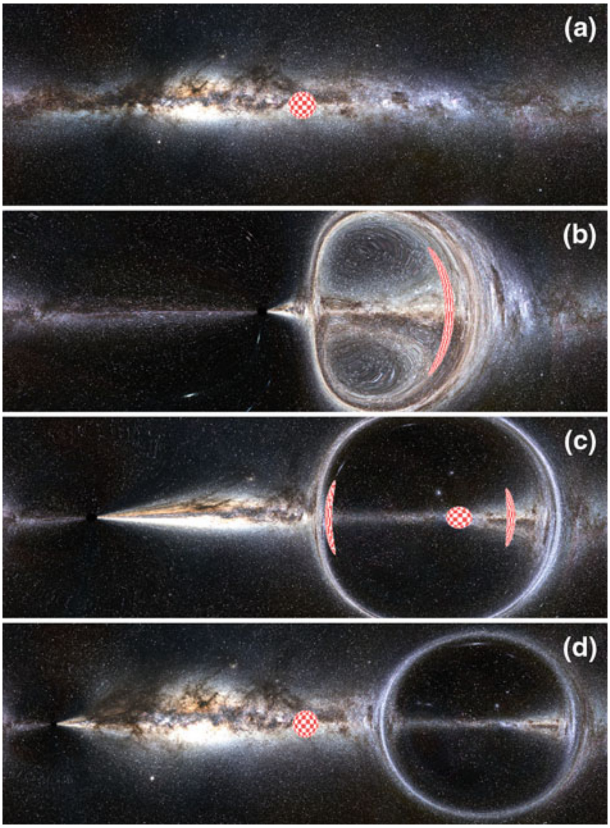

Fig. 11 View of a static observer located at $x = 0$, $y = -4$ in the positive y-direction for $t = 0$ (**a**), $t = 3$ (**b**), $t = 6$ (**c**), and $t = 9$ (**d**). The warp parameters read $R = 2$, $\sigma = 1$, and $v = 2c$. The panorama camera has $180° \times 60°$ field of view. The ball is located at $x = 0$, $y = 3$. Here, only the geometric distortion is shown. The Milky Way background is represented by a sphere with radius $r_{\text{bg}} = 200$

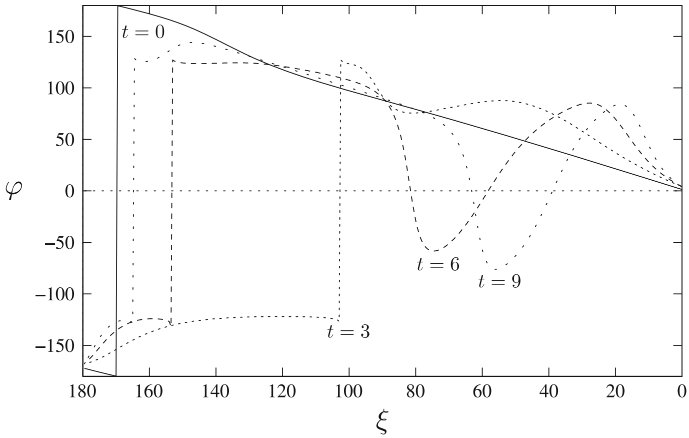

Fig. 12 Angle φ at $r_{\max} = 200$ with respect to incident angle ξ for $t = \{0, 3, 6, 9\}$ and an observer located at $x = 0$, $y = -4$. The warp parameters read $R = 2$, $\sigma = 1$, and $v = 2c$

reflect the apparent horizons at $\xi_{\text{hor}} \approx \{171.3°, 102.8°, 153.6°, 164.8°\}$ for the corresponding observation times $t = \{0, 3, 6, 9\}$. Since the mapping $\varphi \mapsto \xi$ is non-injective, some parts of the sky appears more than once. For example, the point $(r = r_{\max}, \varphi = 50°)$ appears three times at observation time $t = 9$ under the incident angles $\xi \approx \{10.82°, 30.83°, 67.85°\}$.

What can also be read from Fig. 12 is that, after the warp bubble has passed the observer, there is another distortion region that apparently moves in the negative x-direction. This secondary distortion region can be easily understood. Due to the finite speed of light, light rays that have already traversed the warp bubble region at earlier times now reach the observer. Thus, by increasing time, the observer receives ever earlier light rays.

Figure 13 shows the frequency shift for the observation times $t = \{0, 3, 6, 9\}$. At $t = 0$, the frequency shift is negligible. However, when the warp bubble has passed the origin, there is some blue- and redshift from the primary distortion region ($\xi < 90°$), whereas in the secondary region there is a strong redshift close to the apparent horizon directions.

Figure 14 shows the lensing effect for the observation times $t = \{0, 3, 6, 9\}$. Similar to the frequency shift, the magnification at $t = 0$ is negligible. However, when the warp bubble passes the observer, there are strong magnifications at both sides of each bubble rim. In between, stars would appear dimmed. In the regions where the redshift is dominant, the lensing effect fades out the star light.

4 Timelike geodesics

Similar to null geodesics, the trajectories of timelike geodesics are strongly influenced by the warp bubble. Specific to timelike geodesics, particles can now be dragged by the warp bubble and they undergo a geodesic precession. As with null geodesics, we use the non-affinely parametrized geodesic equation with coordinate time as parameter.

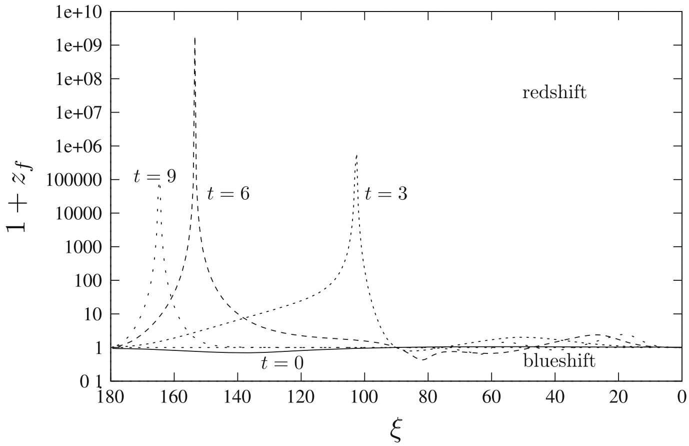

Fig. 13 Frequency shift $1 + z_f$ between $r_{\max} = 200$ and the observer located at $x = 0$, $y = -4$ with respect to incident angle ξ for $t = \{0, 3, 6, 9\}$. The warp parameters read $R = 2$, $\sigma = 1$, and $v = 2c$

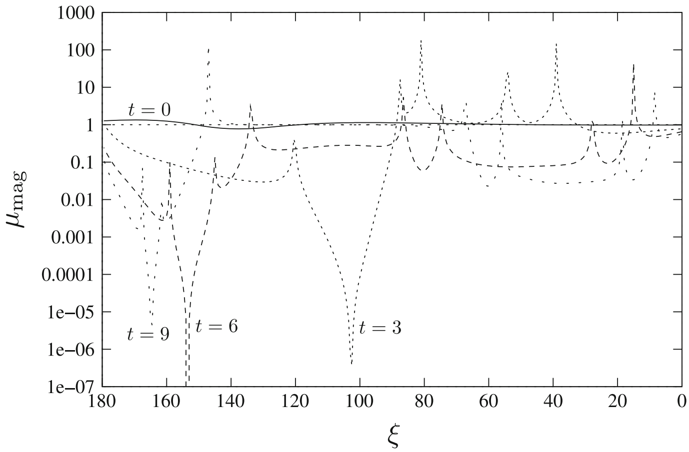

Fig. 14 Magnification μ_{mag} between $r_{\max} = 200$ and the observer located at $x = 0$, $y = -4$ with respect to incident angle ξ for $t = \{0, 3, 6, 9\}$. The warp parameters read $R = 2$, $\sigma = 1$, and $v = 2c$

4.1 Particles from the bridge

A particle at the center of the warp bubble with zero initial velocity will stay there for ever irrespective of the worldline $x(t)$ of the bubble. So, let us consider particles with initial local velocity v_{part} with respect to the comoving reference frame and the corresponding four-velocity

$$\mathbf{u} = c\gamma \left[\mathbf{e}_{(0)} + \beta \left(\cos\xi\,\mathbf{e}_{(1)} + \sin\xi\,\mathbf{e}_{(2)}\right)\right] = u^{\mu}\partial_{\mu}, \tag{13}$$

where $\beta = v_{\text{part}}/c$ and $\gamma = 1/\sqrt{1-\beta^2}$. Figure 15 shows particles that were emitted radially from the bridge with initial local velocity $v_{\text{part}} = 0.5c$. Each solid line

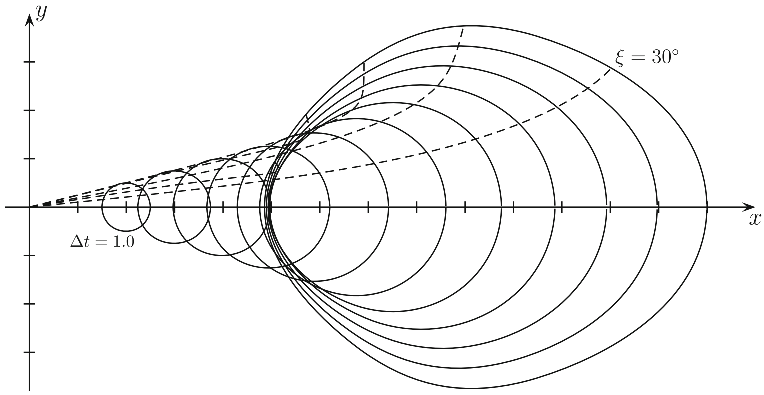

Fig. 15 Particles emitted radially from the bridge with initial local velocity $v_{\text{part}} = 0.5c$ after $\Delta t = \{1.0, 1.5, \ldots, 6.0\}$ (*solid curves*). The dashed lines correspond to particle trajectories for initial directions $\xi = \{30°, \ldots, 150°\}$. The warp parameters read $R = 2$, $\sigma = 1$, $v = 2c$

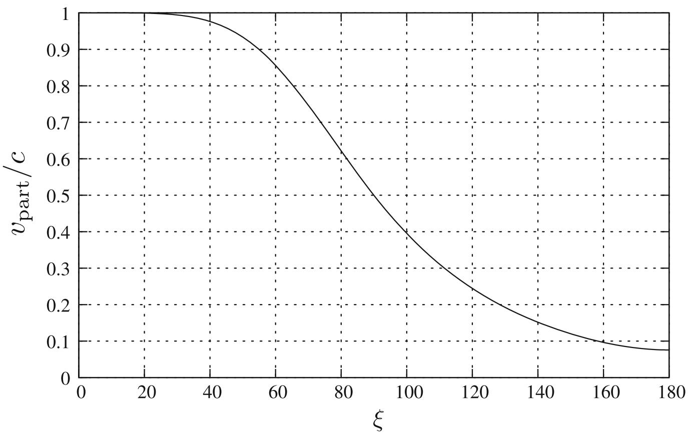

Fig. 16 Particle velocities $v_{\text{part}}(t = 1{,}000)/c$ far outside the bubble's sphere of influence after Δt that were emitted radially from the bridge with initial local velocity $v_{\text{part}}(\tau = 0) = 0.5c$ and initial angles ξ. Particles with initial angles $\xi \lesssim 5°$ are still in the sphere of influence of the warp bubble

represents all particles that have travelled a specific coordinate time Δt. The dashed lines represent particle trajectories for a few initial directions ξ. In the first few seconds, the particles still move within the warp bubble and are carried along with it. Depending on their initial direction ξ, they can leave the warp bubble after some time Δt. To measure the current velocity of a particle during this period, we can use only a valid observer, which is an observer represented by a comoving local tetrad. Such an observer will always measure a velocity less than the speed of light.

Figure 16 shows the velocities of the particles after $\Delta t = 1{,}000$ when all of them are far away from the sphere of influence of the warp bubble. Similar to null geodesics, a particle with initial direction $\xi = 90°$ is only displaced by the warp bubble and the velocity keeps unchanged. All other particles have either a higher or a lower velocity depending on the initial angle ξ.

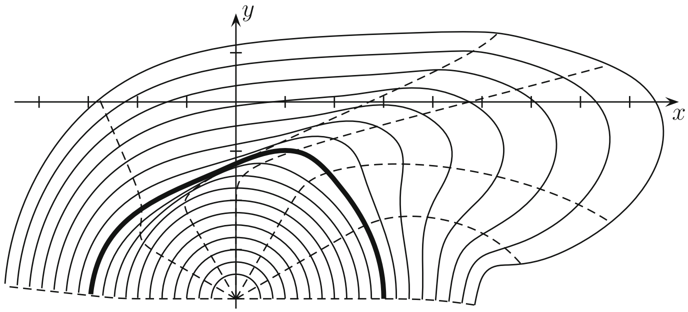

Fig. 17 The solid lines represent particles that start with $\beta = 0.5$ from the position ($t = -6, x = 0, y = -4$). The lines are separated by $\Delta t = 0.5$. The thick solid line indicates $t = 0$. The warp parameters read $R = 2, \sigma = 1, v = 2c$. The dashed lines correspond to timelike geodesics with initial angles $\xi = 0°, 30°, \ldots, 180°$

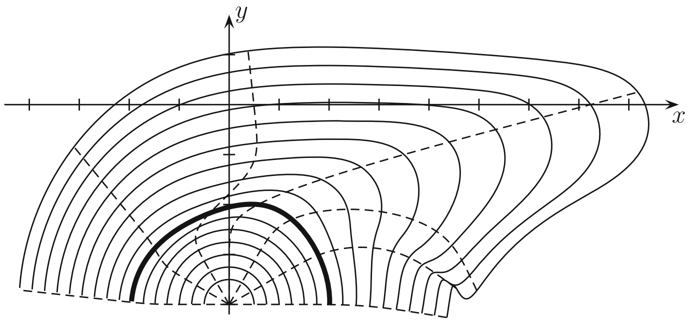

Fig. 18 The same situation as in Fig. 17 but with initial position ($t = -4, x = 0, y = -4$)

4.2 Particles injected from outside

Consider a static observer located at $x = 0$, $y = -4$ that emits particles with local velocity $v_{\text{part}} = 0.5c$ in the directions $\xi \in [0°, 180°]$ at coordinate time t. The corresponding four-velocity $\mathbf{u}$ with respect to the static reference frame reads

$$\mathbf{u} = c\gamma \left[\hat{\mathbf{e}}_{(0)} + \beta \left(\cos\xi\,\hat{\mathbf{e}}_{(1)} + \sin\xi\,\hat{\mathbf{e}}_{(2)}\right)\right] = u^{\mu}\partial_{\mu}, \tag{14}$$

where $\beta = v_{\text{part}}/c$ and $\gamma = 1/\sqrt{1-\beta^2}$. The solid lines of Figs. 17 and 18 show particles that were emitted at coordinate times $t = -6$ or $t = -4$, respectively, and that have travelled some time Δt. The thick solid lines correspond to $t = 0$. The dashed lines represent particle trajectories for a few initial directions ξ.

Depending on the emission time, the particles reach the sphere of influence of the warp bubble under different impact angles. Hence, they will be deflected, carried along, and accelerated or decelerated in different ways.

4.3 Particle field initially at rest

Consider a field of $5 \times 6 = 30$ particles represented by tiny balls that are initially at rest with axes in the positive x direction. The initial position of particle (i, j) is given by $x_i = -3 + i$, $y_j = -4 + j$. At the beginning of the simulation, $t = -3$, the warp bubble with parameters $R = 2, \sigma = 1, v = 2c$ is located at $x = -6, y = 0$. To determine the influence of the warp bubble on this particle field, we calculate the parallel transport of each particle. For that, we have to integrate the geodesic equation with initial conditions $x^\mu\big|_{\tau=0} = (-3, x_i, y_i, 0)\,, dx^\mu/d\tau\big|_{\tau=0} = c\hat{\mathbf{e}}_{(0)}$ together with the parallel-transport equation

$$\frac{dp^\mu}{d\tau} + \Gamma^\mu_{\nu\rho}\frac{dx^\nu}{d\tau}p^\rho = 0, \tag{15}$$

where the four-vector $p^\mu\big|_{\tau=0} = (0, 1, 0, 0)$ describes the orientation of the particle. Like the geodesic equation, we first convert the parallel-transport equation into its non-affinely parametrized form (compare the parallel transport of the Sachs basis vectors explained in “Appendix C”).

When the warp bubble approaches the particle field, the particles will be carried along for some time depending on the distance to the center of the warp bubble, see Fig. 19.

Additionally, the particles undergo a geodesic precession away from the x-axis while they are in the sphere of influence of the warp bubble. The final orientation angle α of a particle axis with respect to the direction of motion is larger the closer the particle is to the x-axis. In the limit $y \to 0$, the maximum change of alpha is $\alpha \to 180°$. Particles at $y = z = 0$, however, keep their orientation.

Figure 20 shows the geodesic precession for particles that initially ($t = -3$) have zero velocity and are located at $x = 0$, $y = \{1, 2, 3\}$. When the particles leave the sphere of influence, they no longer undergo geodesic precession and there is no remaining angular momentum.

5 Geodesics restricted to the x-axis

If we restrict geodesic motion of light rays or particles to the x-axis, the corresponding Lagrangian simplifies to $\mathscr{L} = -c^2\dot{t}^2 + (\dot{x} - vf\dot{t})^2 = \kappa c^2$. In the case of null geodesics, the Euler-Lagrangian equations for $\dot{t}$ and $\dot{x}$ together with the relative coordinate $r = x - vt$, which defines the distance to the center of the warp bubble, Eq. (2), yield

$$\frac{dr}{dt} = \frac{\dot{r}}{\dot{t}} = v\,(f-1) \pm c = v\frac{1-\cosh^2(\sigma r)}{\cosh^2(\sigma r) + \sinh^2(\sigma R)} \pm c. \tag{16}$$

For a future-directed light ray in the positive x direction, we have to use the positive sign. Then, provided that the warp bubble has a velocity $v > 1$ and the initial emission point is at $r(t = 0) = 0$, r approaches r_0 in the limit $t \to \infty$ where the right hand side of Eq. (16) is zero,

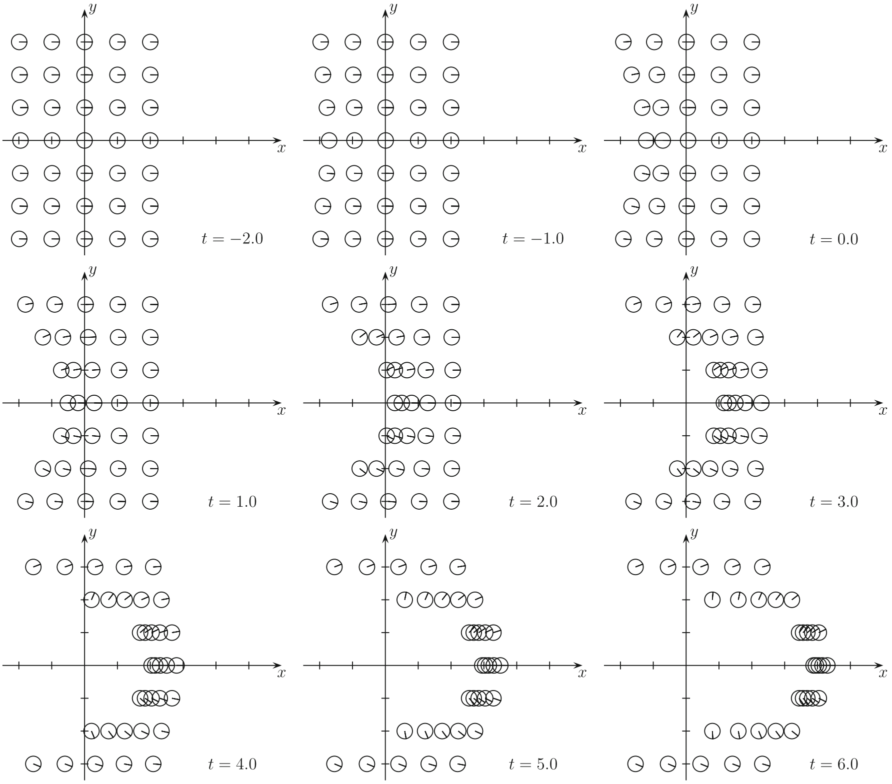

Fig. 19 Parallel transport of tiny balls that are initially ($t = -3$) at rest. The dashes within the balls indicate their orientation. The parameters of the warp metric read $R = 2$, $\sigma = 1$, $v = 2c$

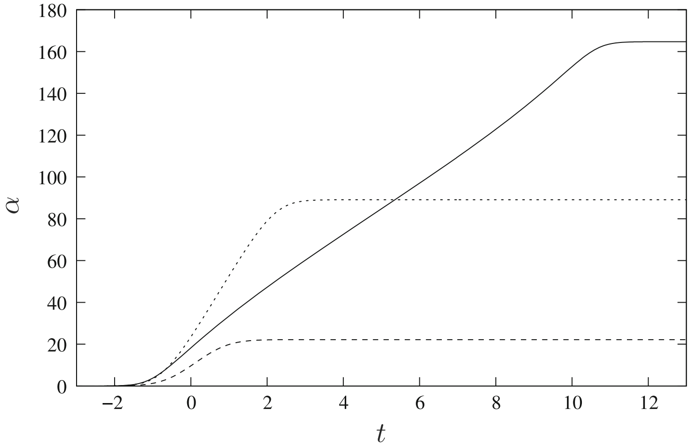

Fig. 20 The orientation α of parallel-transported balls change while they are in the warp bubble's sphere of influence. Here, the initial positions of the balls at $t = -3$ read: $x = 0$ and $y = 1$ (*solid line*), $y = 2$ (*dotted line*), $y = 3$ (*dashed line*). The angle α is measured with respect to a comoving observer, Eq. (3), at the current position of the ball

$$r_0 = \frac{1}{\sigma}\operatorname{arcosh}\left(\sqrt{\frac{c\sinh^2(\sigma R)+v}{v-c}}\right), \qquad f(r_0) = 1-\frac{c}{v}. \tag{17}$$

As expected, the light ray gets stuck within the warp bubble, because light cannot escape from the warp bubble in the direction of motion.

For timelike geodesics, we use the coordinate time t and the relative coordinate r as independent variables. Then, the Lagrangian reads $\mathscr{L} = -c^2\dot{t}^2 + (\dot{r} + v\dot{t} - vf\dot{t})^2 = -c^2$, where now f is independent of t. From the Euler-Lagrangian equations, we obtain the constant of motion $k = [v^2(1-f)^2 - c^2]\dot{t} + v(1-f)\dot{r}$. Thus, the orbital equation reads

$$\frac{dr}{dt} = \frac{\dot{r}}{\dot{t}} = \pm\left[v^2(1-f)^2 - c^2\right]\frac{\sqrt{k^2/c^2 + v^2(1-f)^2 - c^2}}{k \mp v(1-f)\sqrt{k^2/c^2+v^2(1-f)^2-c^2}}. \tag{18}$$

For a particle in the direction of motion that has initial four-velocity $\mathbf{u} = c\gamma(\mathbf{e}_{(0)} + \beta\mathbf{e}_{(1)})$ with respect to an observer at the center of the warp bubble, we have to use the upper sign in Eq. (18) and $k = -\gamma c^2$. In the limit $t \to \infty$, the term $v^2(1-f)^2 - c^2$ dominates the behavior of Eqs. (18) as in (16) and, thus, the particle approaches the same point r_0, Eq. (17), as a light ray irrespective of its initial velocity $\beta > 0$.

Another interesting situation is a particle on the x-axis that is initially at rest with respect to the static local tetrad, Eq. (4), and that will be catched up by an approching warp bubble, compare Sect. 4.3. To determine the particle's velocity β_b with respect to the local reference frame of the bridge, we can use the aforementioned constant of motion k. The warp bubble has velocity $v = 2c$ and crosses the origin $x = 0$ at $t = 0$. The particle has initial position x_i at coordinate time t_i. Then its velocity $\beta_b = -\sqrt{1 - 1/\gamma_b^2}$ follows from

$$\gamma_b = \frac{c^2 + v^2 f_i - f_i^2}{c\sqrt{c^2 - v^2 f_i^2}}, \tag{19}$$

where $f_i = f(r_i) = f(x_i - vt_i)$. Hence, the ball with $x_i = 2$, $y_i = 0$, $t_i = -3$ of Fig. 19 will hit the observer at the bridge with $\beta_b = -0.00714$, but this is only because the ball was already in the bubble's sphere of influence. For a ball that is initially far from that sphere ($r \gg R$), $f_i \to 0$ and thus $\beta_b \to 0$. Hence, such a ball approaches the observer on the bridge only asymptotically and does not traverse the warp bubble.

6 Summary

The Alcubierre warp spacetime offers a rich field for studying geodesics in an extreme application case of general relativity. For a robust and accurate numerical integration of the geodesic equation, the parallel transport, and the Jacobian equation, we have converted these equations into their non-affinely parametrized form, where we've used coordinate time as non-affine parameter.

To a certain degree, the view of an observer comoving with the warp bubble is distorted similarly to the special relativistic aberration. In the direction of motion, however, the distortion is much softer than the special relativistic aberration. Additionally, for velocities larger than the speed of light, there is an apparent horizon behind the warp bubble. However, there is no black region as in the case of the event horizon in the Schwarzschild spacetime. Nevertheless, the strong redshift as well as the large attenuation let the rear side appear extremely dark.

The view of a static observer outside the warp bubble heavily depends on their location and observation time. Light rays are strongly deflected by the warp bubbles and multiple images might appear. Particularly interesting is the purely optical warp bubble that apparently 'moves' contrarily to the actual warp bubble as seen by an outside observer.

Particles that start from inside the warp bubble, will be 'decelerated' or 'accelerated' depending on their initial angle to the warp bubble's direction of motion. Additionally, particles will be dragged and they will undergo geodesic precession while they are in the sphere of influence of the warp bubble.

In this article, we considered only incoming light rays to study the view of an observer for several different situations. A topic of a future publication could be the investigation of outgoing light rays and resulting caustics within either the Alcubierre or, for example, the Van den Broeck [7] Warp metric.

Acknowledgments This work was partially funded by Deutsche Forschungsgemeinschaft (DFG) as part of the Collaborative Research Centre SFB 716 and the DFG project "Astrographik".

Appendix A: Christoffel symbols

The Christoffel symbols of the Alcubierre metric (1) read

$$\begin{aligned}\Gamma^t_{tt} &= \frac{f^2 f_x v^3}{c^2}, \quad \Gamma^y_{tt} = -f f_y v^2, \quad \Gamma^z_{tt} = -f f_z v^2,\\ \Gamma^x_{tt} &= \frac{f^3 f_x v^4}{c^2} - f f_x v^2 - f_t v - f \partial_t v,\end{aligned} \tag{20a}$$

$$\Gamma^t_{tx} = -\frac{f f_x v^2}{c^2}, \Gamma^x_{tx} = -\frac{f^2 f_x v^3}{c^2}, \quad \Gamma^y_{tx} = \frac{f_y v}{2}, \quad \Gamma^z_{tx} = \frac{f_z v}{2}, \tag{20b}$$

$$\begin{aligned}\Gamma^t_{ty} &= -\frac{f f_y v^2}{2c^2}, \Gamma^x_{ty} = -\frac{f^2 f_y v^3 + c^2 f_y v}{2c^2}, \quad \Gamma^t_{tz} = -\frac{f f_z v^2}{2c^2},\\ \Gamma^x_{tz} &= -\frac{f^2 f_z v^3 + c^2 f_z v}{2c^2},\end{aligned} \tag{20c}$$

$$\Gamma^t_{xx} = \frac{f_x v}{c^2}, \Gamma^x_{xx} = \frac{f f_x v^2}{c^2}, \quad \Gamma^t_{xy} = \frac{f_y v}{2c^2}, \quad \Gamma^x_{xy} = \frac{f f_y v^2}{2c^2}, \tag{20d}$$

$$\Gamma^t_{xz} = \frac{f_z v}{2c^2}, \Gamma^x_{xz} = \frac{f f_z v^2}{2c^2}, \tag{20e}$$

with derivatives

$$f_t = \frac{df(r)}{dt} = \frac{-v\,(x - x_s(t))}{r}\frac{df(r)}{dr}, \quad f_x = \frac{df(r)}{dx} = \frac{x - x_s(t)}{r}\frac{df(r)}{dr}, \tag{21a}$$

$$f_y = \frac{df(r)}{dy} = \frac{y}{r}\frac{df(r)}{dr}, \quad f_z = \frac{df(r)}{dz} = \frac{z}{r}\frac{df(r)}{dr}, \tag{21b}$$

and

$$\frac{df(r)}{dr} = \frac{\sigma\left[\operatorname{sech}^2(\sigma(r+R)) - \operatorname{sech}^2(\sigma(r-R))\right]}{2\tanh(\sigma R)}. \tag{22}$$

Appendix B: Geodesic equation

The non-affinely parametrized geodesic equation reads [14]

$$\frac{d^2x^\mu}{d\sigma^2} + \Gamma^\mu_{\nu\rho}\frac{dx^\nu}{d\sigma}\frac{dx^\rho}{d\sigma} = -\frac{1}{\zeta(\sigma)}\frac{d\zeta(\sigma)}{d\sigma}\frac{dx^\mu}{d\sigma}, \tag{23}$$

where σ is an arbitrary (non-affine) parameter and ζ is a function of σ. The affine parameter λ then follows from

$$\lambda = \int\limits_{\sigma_0}^{\sigma} \frac{a}{\zeta(\sigma)} d\sigma, \tag{24}$$

with

$$\frac{d\sigma}{d\lambda} = \frac{\zeta(\sigma)}{a}, \qquad \frac{d^2\sigma}{d\lambda^2} = \frac{1}{a}\frac{d\zeta}{d\sigma}\frac{d\sigma}{d\lambda}, \tag{25}$$

and an arbitrary but constant factor a. The relation between the affinely and the non-affinely parametrized geodesic equations can be derived by means of the chain rule

$$\frac{dx^\mu}{d\lambda} = \frac{dx^\mu}{d\sigma}\frac{d\sigma}{d\lambda}, \qquad \frac{d^2x^\mu}{d\lambda^2} = \frac{d^2x^\mu}{d\sigma^2}\left(\frac{d\sigma}{d\lambda}\right)^2 + \frac{dx^\mu}{d\sigma}\frac{d^2\sigma}{d\lambda^2}. \tag{26}$$

If we replace the non-affine parameter σ by the coordinate time t, Eq. (23) with $x^0 = t$ yields

$$\Gamma^0_{\nu\rho}\frac{dx^\nu}{dt}\frac{dx^\rho}{dt} = -\frac{1}{\zeta(t)}\frac{d\zeta(t)}{dt}. \tag{27}$$

Thus, the geodesic equation (23) can be written as

$$\frac{d^2x^i}{dt^2} + \Gamma^i_{\nu\rho}\frac{dx^\nu}{dt}\frac{dx^\rho}{dt} = \Gamma^0_{\nu\rho}\frac{dx^\nu}{dt}\frac{dx^\rho}{dt}\frac{dx^i}{dt}, \tag{28}$$

which simplifies to

$$0 = \frac{d^2x^i}{dt^2} - \frac{dx^i}{dt}\left(\Gamma^0_{00} + 2\Gamma^0_{0j}\frac{dx^j}{dt} + \Gamma^0_{jk}\frac{dx^j}{dt}\frac{dx^k}{dt}\right) + \Gamma^i_{00} + 2\Gamma^i_{0j}\frac{dx^j}{dt} + \Gamma^i_{jk}\frac{dx^j}{dt}\frac{dx^k}{dt}, \tag{29}$$

where $i = 1, 2, 3$ and summation indices j, k go from 1 to 3. The generalization of the constraint equation, $g_{\mu\nu}(dx^\mu/d\lambda)(dx^\nu/d\lambda) = \kappa c^2$ with $\kappa = 0$ for lightlike and $\kappa = -1$ for timelike geodesics, reads

$$\left(\frac{dt}{d\lambda}\right)^2\left(g_{00} + 2g_{0i}\frac{dx^i}{dt} + g_{ij}\frac{dx^i}{dt}\frac{dx^j}{dt}\right) = \kappa c^2. \tag{30}$$

The function ζ follows from Eq. (27):

$$\zeta(t) = \zeta_0 \exp\left[-\int_{t_0}^{t} \Gamma^0_{00} + \Gamma^0_{0i}\frac{dx^i}{dt'} + \Gamma^0_{ij}\frac{dx^i}{dt'}\frac{dx^j}{dt'}dt'\right]. \tag{31}$$

Details about the numerical implementation are given in "Appendix E".

Appendix C: Parallel transport of Sachs basis and Jacobi equation

The parallel transport equation for the Sachs basis vector $\mathbf{s} = s^\mu\partial_\mu$ can be cast into the form

$$0 = \frac{ds^\mu}{dt} + \left(\Gamma^\mu_{0\nu} + \Gamma^\mu_{i\nu}\frac{dx^i}{dt}\right)s^\nu. \tag{32}$$

The Jacobian equation for the Jacobian field $\mathbf{Y} = Y^\mu\partial_\mu$ reads

$$0 = \frac{d^2Y^\mu}{dt^2} - \frac{dY^\mu}{dt}\left(\Gamma^0_{00} + 2\Gamma^0_{0j}\frac{dx^j}{dt} + \Gamma^0_{jk}\frac{dx^j}{dt}\frac{dx^k}{dt}\right) + 2\left(\Gamma^\mu_{0\nu} + \Gamma^\mu_{i\nu}\frac{dx^i}{dt}\right)\frac{dY^\nu}{dt} + \left(\Gamma^\mu_{00,\nu} + 2\Gamma^\mu_{0i,\nu}\frac{dx^i}{dt} + \Gamma^\mu_{ij,\nu}\frac{dx^i}{dt}\frac{dx^j}{dt}\right)Y^\nu. \tag{33}$$

The initial Sachs basis vectors are perpendicular to the initial light direction $\mathbf{k} = -\mathbf{e}_{(0)} + \cos\xi\,\mathbf{e}_{(1)} + \sin\xi\,\mathbf{e}_{(2)}$, thus

$$\mathbf{s}_1 = -\sin\xi\,\mathbf{e}_{(1)} + \cos\xi\,\mathbf{e}_{(2)} \quad \text{and} \quad \mathbf{s}_2 = \mathbf{e}_{(3)}. \tag{34}$$

The initial values for the two Jacobian fields read $Y^{\mu}_{1,2}\big|_{t=0} = 0$ and $dY^{\mu}_{1,2}/dt\big|_{t=0} = s^{\mu}_{1,2}$. Details about the numerical implementation are given in "Appendix E".

Appendix D: Euler-Lagrange equations

The Euler-Lagrange [15] equations for geodesics in the $z = \text{const}$ hyperplane with Lagrangian

$$\mathscr{L} = -c^2\dot{t}^2 + \left(\dot{x} - vf\dot{t}\right)^2 + \dot{y}^2 \tag{35}$$

and $v = \text{const}$ yield

$$0 = \frac{d}{d\lambda}\left[c^2\dot{t} + vf\left(\dot{x} - vf\dot{t}\right)\right] - \left(\dot{x} - vf\dot{t}\right)\dot{t}vf_t, \tag{36a}$$

$$0 = \frac{d}{d\lambda}\left[\dot{x} - vf\dot{t}\right] + \left(\dot{x} - vf\dot{t}\right)v\dot{t}f_x, \tag{36b}$$

$$0 = \ddot{y} + \left(\dot{x} - vf\dot{t}\right)v\dot{t}f_y, \tag{36c}$$

where a dot means differentiation with respect to the affine parameter λ. It is obvious that these equations are automatically fulfilled for

$$\dot{t} = k_1, \quad \dot{x} = vfk_1, \quad \dot{y} = k_2, \tag{37}$$

with constants of motion k_1 and k_2. These initial values correspond to a null or timelike geodesic that starts perpendicular to the direction of motion with respect to the comoving reference frame of the center of the bubble. Because y grows linearly, the shape function f tends to zero and, thus, x is limited. Hence, such a geodesic approaches a line orthogonal to the x-axis.

In case of a null geodesic, the initial direction reads $\mathbf{k} = \omega\left(\pm\mathbf{e}_{(0)} + \mathbf{e}_{(2)}\right)$, which yields $k_1 = \pm\omega/c$ and $k_2 = \omega$. Thus, there is no frequency shift. A timelike geodesic with initial local velocity v_{part} and four-velocity $\mathbf{u} = c\gamma(\mathbf{e}_{(0)} + \beta\mathbf{e}_{(2)})$, where $\beta = v_{\text{part}}/c$ and $\gamma = 1/\sqrt{1-\beta^2}$, has constants of motion $k_1 = \gamma$ and $k_2 = \gamma\beta c$.

Appendix E: Numerical integration

The integration of the non-affinely parametrized geodesic equation avoids the problem of the inadequate affine parameter. However, we still need the affine parameter for the calculation of the magnification factor. From Eqs. (24) and (27) we can expand the set of ordinary differential equations for λ to

$$\frac{d\lambda}{dt} = \frac{a}{\zeta}, \qquad \frac{d\zeta}{dt} = \left(-\Gamma^0_{00} - 2\Gamma^0_{0i}\frac{dx^i}{dt} - \Gamma^0_{ij}\frac{dx^i}{dt}\frac{dx^j}{dt}\right)\zeta. \tag{38}$$

Since ζ grows exponentially, which results in numerical problems, we substitute $\zeta = \exp(\psi)$ in (38) and obtain

$$\frac{d\psi}{dt} = -\Gamma^0_{00} - 2\Gamma^0_{0i}\frac{dx^i}{dt} - \Gamma^0_{ij}\frac{dx^i}{dt}\frac{dx^j}{dt}. \tag{39}$$

Here, we set $a = 1$. Numerical problems due to exponential grow of the Sachs vectors and the Jacobi functions make the following substitutions necessary: $s^\mu = \sinh(p^\mu)$, $Y^\mu = \sinh(u^\mu)$. The parallel transport of the Sachs vectors then reads

$$\frac{dp^\mu}{dt} = -\left(\Gamma^\mu_{0\sigma} + \Gamma^\mu_{i\sigma}\frac{dx^i}{dt}\right)\frac{\sinh(p^\sigma)}{\cosh(p^\mu)}. \tag{40}$$

Note that there is no summation over the index μ in the right hand side of this equation. For the integration of the Jacobian equation (33), we obtain

$$\frac{du^\mu}{dt} = w^\mu, \tag{41a}$$

$$\begin{aligned}\frac{dw^\mu}{dt} &= -\tanh(u^\mu)\left(w^\mu\right)^2 + \left(\Gamma^0_{00} + 2\Gamma^0_{0j}\frac{dx^j}{dt} + \Gamma^0_{jk}\frac{dx^j}{dt}\frac{dx^k}{dt}\right)w^\mu \\ &\quad - 2\left(\Gamma^\mu_{0\nu} + \Gamma^\mu_{i\nu}\frac{dx^i}{dt}\right)\frac{\cosh(u^\nu)}{\cosh(u^\mu)}w^\mu \\ &\quad - \left(\Gamma^\mu_{00,\nu} + 2\Gamma^\mu_{0i,\nu}\frac{dx^i}{dt} + \Gamma^\mu_{ij,\nu}\frac{dx^i}{dt}\frac{dx^j}{dt}\right)\frac{\sinh(u^\nu)}{\cosh(u^\mu)}.\end{aligned} \tag{41b}$$

As before, there is no summation over the index μ.

To apply numerical libraries like, for example, the GNU Scientific Library [16] or the Numerical Recipes [17], we have to map the above equations to a one-dimensional array as follows:

$$\mathrm{y}[n] = x^{n+1}, \quad \mathrm{y}[n+3] = \frac{dx^{n+1}}{dt}, \quad \mathrm{y}[m+6] = p_1^m, \mathrm{y}[m+10] = p_2^m, \tag{42a}$$

$$\mathrm{y}[m+14] = Y_1^m, \quad \mathrm{y}[m+18] = \frac{dY_1^m}{dt}, \quad \mathrm{y}[m+22] = Y_1^m, \quad \mathrm{y}[m+26] = \frac{dY_1^m}{dt}, \tag{42b}$$

$$\mathrm{y}[30] = \psi, \quad \mathrm{y}[31] = \lambda. \tag{42c}$$

Here, $n = 0, 1, 2$ and $m = 0, 1, 2, 3$.

A light ray with initial direction $\mathbf{k} = \pm\mathbf{e}_{(0)} + \cos\xi\,\mathbf{e}_{(1)} + \sin\xi\,\mathbf{e}_{(2)}$yields $\dot{t} = \pm 1/c$, $\dot{x} = \pm vf/c + \cos\xi$, and $\dot{y} = \sin\xi$. Thus $\mathtt{y}[3] = \dot{x}/\dot{t} = vf \pm c\cos\xi$, $\mathtt{y}[4] = \pm c\sin\xi$, and $\mathtt{y}[5] = 0$. The corresponding Sachs vectors (34) give $\mathtt{y}[6] = \mathtt{y}[9] = 0$, $\mathtt{y}[7] = \operatorname{arsinh}(-\sin\xi)$, $\mathtt{y}[8] = \operatorname{arsinh}(\cos\xi)$, $\mathtt{y}[10] = \mathtt{y}[11] = \mathtt{y}[12] = 0$, and $\mathtt{y}[13] = \operatorname{arsinh}(-1)$. The initial values for the Jacobi vector fields are obvious. For the integration of the affine parameter λ with $\lambda(0) = 0$, we have $\zeta(0) = 1$ and $\psi(0) = 0$. Hence, $\mathtt{y}[30] = \mathtt{y}[31] = 0$.

For the numerical integration of timelike geodesics, we can reduce the system (42) to only eight equations. The array elements $\mathtt{y}[]$ can then be deduced from the following equations. Particles from the bridge have initial directions

$$\frac{dt}{d\lambda} = \gamma, \quad \frac{dx}{dt} = vf + c\beta\cos\xi, \quad \frac{dy}{dt} = c\beta\sin\xi, \tag{43}$$

whereas particles injected from a static outside observer are described by

$$\begin{aligned}\frac{dt}{d\lambda} &= \frac{c\gamma}{\sqrt{c^2 - v^2 f^2}}(1 - \beta vf\cos\xi),\\ \frac{dx}{dt} &= \gamma\beta\sqrt{c^2 - v^2 f^2}\cos\xi, \quad \frac{dy}{dt} = c\gamma\beta\sin\xi.\end{aligned} \tag{44}$$

In both cases, we have $\psi(0) = \ln\gamma$.

References

1. Morris, M.S., Thorne, K.S.: Wormholes in spacetime and their use for interstellar travel: a tool for teaching general relativity. Am. J. Phys. **56**, 395–412 (1988)
2. Alcubierre, M.: The warp drive: hyper-fast travel within general relativity. Class. Quantum Grav. **11**, L73–L77 (1994)
3. Clark, C., Hiscock, W.A., Larson, S.L.: Null geodesics in the Alcubierre warp-drive spacetime: the view from the bridge. Class. Quantum Grav. **16**, 3965–3972 (1999)
4. Weiskopf, D.: Four-dimensional non-linear ray tracing as a visualization tool for gravitational physics.In: Proceedings of the IEEE Conference on Visualization, IEEE Computer Society Press, 2000, pp. 445–448
5. Hiscock, W.A.: Quantum effects in the Alcubierre warp-drive spacetime. Class. Quantum Grav. **14**, L183–L188 (1997)
6. Pfenning, M.J., Ford, L.H.: The unphysical nature of 'warp drive'. Class. Quantum Grav. **14**, 1743–1751 (1997)
7. van den Broeck, C.: A 'warp drive' with more reasonable total energy requirements. Class. Quantum Grav. **16**, 3973–3979 (1999)
8. Lobo, F.S.N., Visser, M.: Fundamental limitations on 'warp drive' spacetimes. Class. Quantum Grav. **21**, 5871–5892 (2004)
9. Müller, T., Grave, F.: GeodesicViewer—a tool for exploring geodesics in the theory of relativity. Comput. Phys. Commun. **181**, 413–419 (2010)
10. Wald, R.M.: General relativity. The University of Chicago Press, Chicago (1984)
11. Schneider, P., Ehlers, J., Falco, E.E.: Gravitational Lenses. Springer, Berlin (1992)
12. The Milky Way panorama is by ESO/S. Brunier, http://www.eso.org/public/images/eso0932a
13. Weiskopf, D., Kraus, U., Ruder, H.: Searchlight and doppler effects in the visualization of special relativity: a corrected derivation of the transformation of radiance. ACM Trans. Graph. **18**, 278–292 (1999)
14. Nwankwo, A., Thompson, J., Ishak, M.: Luminosity distance and redshift in the Szekeres inhomogeneous cosmological models. arXiv:1005.2989v1 [astro-ph]

15. Rindler, W.: Relativity—Special, General and Cosmology. Oxford University Press, Oxford (2001)
16. GNU Scientific Library (GSL), http://www.gnu.org/software/gsl
17. Press, W.H., Teukolsky, S.A., Vetterling, W.T., Flannery, B.P.: Numerical Recipes in C. Cambridge University Press, Cambridge (2002)